Journal of
Biomedical Optics

SPIEDigitalLibrary.org/jbo

Multispectral imaging of absorption and scattering properties of *in vivo* exposed rat brain using a digital red-green-blue camera

Keiichiro Yoshida
Izumi Nishidate
Tomohiro Ishizuka
Satoko Kawauchi
Shunichi Sato
Manabu Sato

SPIE

Journal of Biomedical Optics 20(5), 051026 (May 2015)

Multispectral imaging of absorption and scattering properties of *in vivo* exposed rat brain using a digital red-green-blue camera

Keiichiro Yoshida,[a] Izumi Nishidate,[a,*] Tomohiro Ishizuka,[a] Satoko Kawauchi,[b] Shunichi Sato,[b] and Manabu Sato[c]
[a]Tokyo University of Agriculture & Technology, Graduate School of Bio-Application & Systems Engineering, Koganei, Tokyo 184-8588, Japan
[b]National Defense Medical College Research Institute, Division of Biomedical Information Sciences, Tokorozawa, Saitama 359-8513, Japan
[c]Yamagata University, Graduate School of Science and Engineering, Yonezawa, Yamagata 992-8510, Japan

Abstract. In order to estimate multispectral images of the absorption and scattering properties in the cerebral cortex of *in vivo* rat brain, we investigated spectral reflectance images estimated by the Wiener estimation method using a digital RGB camera. A Monte Carlo simulation-based multiple regression analysis for the corresponding spectral absorbance images at nine wavelengths (500, 520, 540, 560, 570, 580, 600, 730, and 760 nm) was then used to specify the absorption and scattering parameters of brain tissue. In this analysis, the concentrations of oxygenated hemoglobin and that of deoxygenated hemoglobin were estimated as the absorption parameters, whereas the coefficient a and the exponent b of the reduced scattering coefficient spectrum approximated by a power law function were estimated as the scattering parameters. The spectra of absorption and reduced scattering coefficients were reconstructed from the absorption and scattering parameters, and the spectral images of absorption and reduced scattering coefficients were then estimated. In order to confirm the feasibility of this method, we performed *in vivo* experiments on exposed rat brain. The estimated images of the absorption coefficients were dominated by the spectral characteristics of hemoglobin. The estimated spectral images of the reduced scattering coefficients had a broad scattering spectrum, exhibiting a larger magnitude at shorter wavelengths, corresponding to the typical spectrum of brain tissue published in the literature. The changes in the estimated absorption and scattering parameters during normoxia, hyperoxia, and anoxia indicate the potential applicability of the method by which to evaluate the pathophysiological conditions of *in vivo* brain due to the loss of tissue viability. [DOI: 10.1117/1.JBO.20.5.051026]

Keywords: multispectral imaging; Wiener estimation method; diffuse reflectance spectroscopy; Monte Carlo simulation; multiple regression analysis; reduced scattering coefficient; absorption coefficient.

Paper 140482SSR received Jul. 25, 2014; accepted for publication Dec. 29, 2014; published online Jan. 23, 2015.

1 Introduction

Evaluating the optical properties of brain tissue is important for the application of light in clinical diagnosis, surgery, and therapeutic procedures for brain diseases. The optical properties of biological tissue have been used to evaluate spatial and/or temporal changes of neuronal activity and tissue viability in the brain as intrinsic optical signals (IOSs). IOSs in the brain are believed to be caused primarily by the following processes: hemodynamic-related changes in absorption and scattering properties, changes in absorption due to redox states of cytochromes in mitochondria, changes in scattering generated by cell swelling or shrinkage caused by water movement between intracellular and extracellular compartments,[1] and changes in scattering and absorption caused by chromophore contents and cell deformations. Light in the visible to near-infrared spectral range is sensitive to the absorption and scattering properties of biological tissue. The absorption and scattering properties of *in vitro* tissue slices can be estimated from the measured diffuse reflectance and transmittance of tissue slices[2] based on several light transport models, such as the Kubelka-Munk theory,[3] the diffusion approximation to the transport equation,[4] the Monte Carlo method,[5] and the adding-doubling method.[6] Numerous spectroscopic methods have been investigated for *in vivo* determination of the scattering and absorption properties in living tissues, including time-resolved measurements,[7] a frequency-domain method,[8] and spatially resolved measurements with continuous wave (CW) light.[9–15]

Diffuse reflectance spectroscopy (DRS) based on the measurement of CW light can be simply achieved with an incandescent white light source, inexpensive optical components, and a spectrometer. DRS is one of the most promising methods for evaluating the absorption and scattering properties of *in vivo* brain tissue. Several approaches using a Monte Carlo simulation-based lookup table have been investigated for determining the absorption and scattering properties of biological tissue.[16–19] Several imaging methods based on DRS have been used to investigate cortical hemodynamics based on changes in the absorption properties of brain tissue.[20–24] In order to achieve rapid multispectral imaging, the use of an acousto-optical tunable filter[25] and the combination of a lenslet array with narrowband filters[26] have been proposed. On the other hand, the reconstruction of multispectral images from a red green blue (RGB) image acquired by a digital RGB camera is promising as a method of rapid and cost-effective multispectral imaging. Several reconstruction techniques for multispectral images, such

---

*Address all correspondence to: Izumi Nishidate, E-mail: inishi@cc.tuat.ac.jp

as the pseudo-inverse method,[27–30] finite-dimensional modeling,[29,31] the nonlinear estimation method,[32] and the Wiener estimation method (WEM),[33–35] have been investigated. Among these reconstruction techniques, the WEM is one of the most promising methods for practical applications because of its simplicity, cost-effectiveness, accuracy, time efficiency, and the possibility of high-resolution image acquisition.

In the present study, we investigate a simple spectral imaging of reduced scattering coefficients $\mu_s'(\lambda)$ and the absorption coefficients $\mu_a(\lambda)$ of *in vivo* exposed brain tissues in the range of wavelengths from visible to near-infrared based on DRS using a multispectral imaging system. Multispectral diffuse reflectance images of *in vivo* exposed brain are estimated from an RGB image captured by a digital RGB camera. The Monte Carlo simulation-based multiple regression analysis for the estimated absorbance spectra at nine wavelengths (500, 520, 540, 560, 570, 580, 600, 730, and 760 nm) is then used to specify the concentrations of oxygenated and deoxygenated hemoglobin as the absorption parameters, and the coefficient a and the exponent b of the reduced scattering coefficient spectrum approximated by a power law function as the scattering parameters. The absorption coefficient spectrum and the reduced scattering coefficient spectrum are finally reconstructed from the hemoglobin concentrations and the scattering parameters, respectively. In order to confirm the feasibility of a method by which to evaluate the absorption and scattering properties of the cerebral cortex, we performed *in vivo* experiments using exposed rat brain while changing the fraction of inspired oxygen ($\mathrm{FiO_2}$).

2 Principle

2.1 Estimation of Spectral Diffuse Reflectance Images by Wiener Estimation

The response of a digital color camera in spatial coordinates (x, y) with the i'th $(i = 1, 2, 3)$ color channel, or red, green, and blue can be calculated as

$$v_i(x,y) = \int u_i(\lambda)E(\lambda)S(\lambda)r(x,y;\lambda)\mathrm{d}\lambda, \tag{1}$$

where λ is the wavelength, $u_i(\lambda)$ is the transmittance spectrum of the i'th filter, $E(\lambda)$ is the spectrum of the illuminant, $S(\lambda)$ is the sensitivity of the camera, and r $(x, y; \lambda)$ is the reflectance spectrum in the spatial coordinates (x, y). For convenience, Eq. (1) is expressed in discrete vector notation as

$$\mathbf{v} = \mathbf{Fr}, \tag{2}$$

where $\mathbf{v}$ is a vector having a three-element column and $\mathbf{r}$ is a vector having a k-element column, which corresponds to the reflectance spectrum of a pixel of an image. Moreover, $\mathbf{F}$ is a $3 \times k$ matrix and is expressed as

$$\mathbf{F} = \mathbf{UES}, \tag{3}$$

where $\mathbf{U} = [u_1, u_2, u_3]^T$. Column vector u_i denotes the transmittance spectrum of the i'th filter, and $[\,]^T$ represents the transposition of a vector. Also, $\mathbf{E}$ and $\mathbf{S}$ are $k \times k$ diagonal matrices representing the spectrum of the illuminant and the sensitivity of the camera, respectively. The Wiener estimation[33–35] of $\mathbf{r}$ is given by

$$\tilde{\mathbf{r}} = \mathbf{Wv}, \tag{4}$$

where $\mathbf{W}$ is the Wiener estimation matrix. The purpose of $\mathbf{W}$ is to minimize the minimum square error between the original and estimated reflectance spectra. In this case, the minimum square error is expressed as

$$e = \langle(\mathbf{r} - \tilde{\mathbf{r}})^t(\mathbf{r} - \tilde{\mathbf{r}})\rangle. \tag{5}$$

From Eqs. (4) and (5), the minimum square error is rewritten as

$$\begin{aligned} e &= \langle(\mathbf{r} - \tilde{\mathbf{r}})^t(\mathbf{r} - \tilde{\mathbf{r}})\rangle \\ &= \langle\mathbf{r}^t\mathbf{r}\rangle - \mathbf{W}\langle\mathbf{r}^t\mathbf{v}\rangle - \mathbf{W}^t\langle\mathbf{v}^t\mathbf{r}\rangle + \mathbf{W}^t\mathbf{W}\langle\mathbf{v}^t\mathbf{v}\rangle. \end{aligned} \tag{6}$$

The minimization of the minimum square error requires that the partial derivative of e with respect to $\mathbf{W}$ be zero, i.e.,

$$\frac{\partial e}{\partial \mathbf{W}} = -\langle\mathbf{r}^t\mathbf{v}\rangle + \mathbf{W}^t\langle\mathbf{v}^t\mathbf{v}\rangle = 0. \tag{7}$$

From Eq. (7), the matrix $\mathbf{W}$ is derived as

$$\mathbf{W} = \langle\mathbf{rv}^T\rangle\langle\mathbf{vv}^T\rangle^{-1} = \langle\mathbf{rv}^T\rangle\mathbf{F}^T(\mathbf{F}\langle\mathbf{rr}^T\rangle\mathbf{F}^T)^{-1}, \tag{8}$$

where $\langle\,\rangle$ is an ensemble-averaging operator. The derivation of matrix $\mathbf{W}$ requires the autocorrelation matrix $\langle\mathbf{rr}^T\rangle$. In the present study, we determine $\langle\mathbf{rr}^T\rangle$ based on 720 different reflectance spectra obtained from *in vivo* rat brain under various physiological conditions.

To test the accuracy in spectral reconstruction, the estimated spectrum at 27 different wavelengths by WEM was compared with the measured spectrum by spectrometer using a goodness-of-fit coefficient (GFC).[36] The GFC is based on the inequality of Schwartz and it is described as

$$\mathrm{GFC} = \frac{|\sum_j r_{\mathrm{mes}}(\lambda_j) r_{\mathrm{est}}(\lambda_j)|}{\sqrt{|\sum_j [r_{\mathrm{mes}}(\lambda_j)]^2|}\sqrt{|\sum_j [r_{\mathrm{est}}(\lambda_j)]^2|}}, \tag{9}$$

where $r_{\mathrm{meas}}(\lambda_i)$ is the measured original spectral data at the wavelength λ_I and $r_{\mathrm{est}}(\lambda_i)$ is the estimated spectral data at the wavelength λ_i. Hernández-Andrés et al.[36] suggested that colorimetrically accurate $r_{\mathrm{meas}}(\lambda_i)$ requires a $\mathrm{GFC} > 0.995$; a "good" spectral fit requires a $\mathrm{GFC} \geq 0.999$, and $\mathrm{GFC} \geq 0.9999$ is necessary for an "excellent" spectral fit.

2.2 Estimation of the Absorption Coefficient and the Reduced Scattering Coefficient

Figure 1 shows a flow diagram of the method used to estimate the absorption coefficient $\mu_a(\lambda)$ and the reduced scattering coefficient $\mu_s'(\lambda)$. The absorbance spectrum $A(\lambda)$ is defined as

$$A(\lambda) = -\log_{10} r(\lambda), \tag{10}$$

where $r(\lambda)$ is the diffuse reflectance spectrum normalized by the incident light spectrum. Since attenuation due to light scattering can be treated as a pseudochromophore, the absorbance spectrum $A(\lambda)$ can be approximated as the sum of attenuations due to absorption and scattering in the brain as

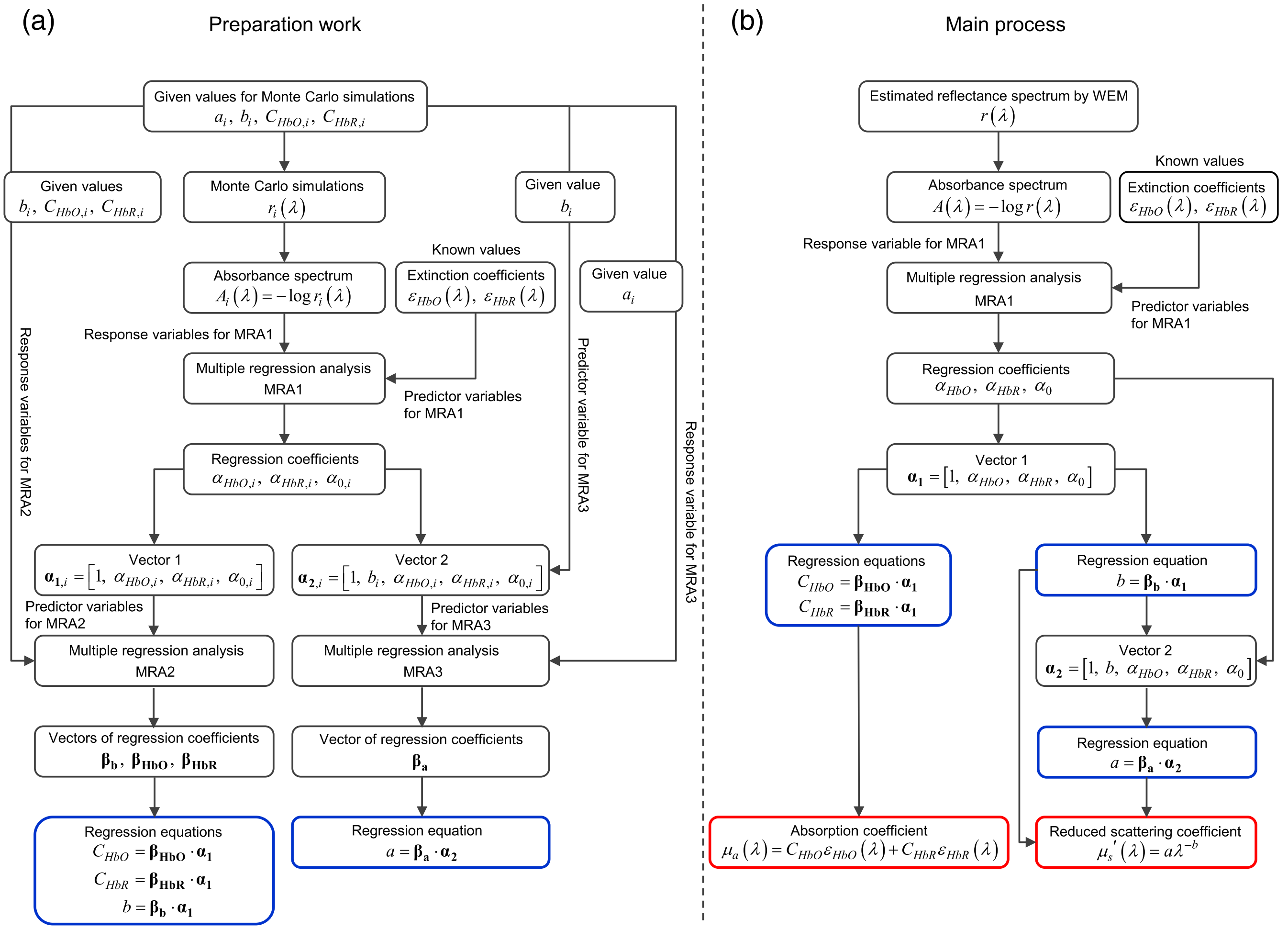

Fig. 1 Flow diagram of the process for estimating the concentration of oxygenated hemoglobin C_{HbO}, the concentration of deoxygenated hemoglobin C_{HbR}, coefficient *a*, exponent *b*, absorption coefficient $\mu_a(\lambda)$, and reduced scattering coefficient $\mu_s'(\lambda)$. (a) Preparation work for determining the regression equations and (b) main process for deriving $\mu_a(\lambda)$ and $\mu_s'(\lambda)$ from the reflectance spectrum $r(\lambda)$ estimated by the Wiener estimation method (WEM).

$$A(\lambda) = C_{\mathrm{HbO}} l(\lambda, C_{\mathrm{HbO}}, C_{\mathrm{HbR}}, \mu_s')\varepsilon_{\mathrm{HbO}}(\lambda) + C_{\mathrm{HbR}} l(\lambda, C_{\mathrm{HbO}}, C_{\mathrm{HbR}}, \mu_s')\varepsilon_{\mathrm{HbR}}(\lambda) + D(\lambda, \mu_s'), \tag{11}$$

where C is the concentration, l is the mean path length, $\varepsilon(\lambda)$ is the extinction coefficient, and $D(\lambda, \mu_s')$ indicates attenuation due to light scattering in the tissue. The subscripts HbO and HbR denote oxygenated hemoglobin and deoxygenated hemoglobin, respectively. The absorption coefficient of the cortical tissue was assumed to depend only on the concentrations of HbO and HbR (C_{HbO}, C_{HbR}) as

$$\mu_a(\lambda) = C\varepsilon(\lambda) = C_{\mathrm{HbO}}\varepsilon_{\mathrm{HbO}}(\lambda) + C_{\mathrm{HbR}}\varepsilon_{\mathrm{HbR}}(\lambda). \tag{12}$$

The total hemoglobin concentration C_{HbT} is defined as the sum of C_{HbO} and C_{HbR} as follows:

$$C_{\mathrm{HbT}} = C_{\mathrm{HbO}} + C_{\mathrm{HbR}}. \tag{13}$$

The tissue oxygen saturation is determined as

$$\mathrm{StO_2}[\%] = 100 \times \frac{C_{\mathrm{HbO}}}{C_{\mathrm{HbT}}}. \tag{14}$$

The reduced scattering coefficient of the brain tissue was assumed to take the following form as a power law function:[37,38]

$$\mu_s'(\lambda) = a\lambda^{-b}, \tag{15}$$

where the coefficient a and the exponent b represent the scattering amplitude and the scattering power, respectively. Using $A(\lambda)$ as the response variable and $\varepsilon(\lambda)$ as the predictor variables, the multiple regression analysis based on the modified Lambert-Beer law (MRA1) can be applied to Eq. (11) as

$$A(\lambda) = \alpha_{\mathrm{HbO}}\varepsilon_{\mathrm{HbO}}(\lambda) + \alpha_{\mathrm{HbR}}\varepsilon_{\mathrm{HbR}}(\lambda) + \alpha_0, \tag{16}$$

where α_{HbO}, α_{HbR}, and α_0 are the regression coefficients. The regression coefficients α_{HbO} and α_{HbR} describe the degree of contribution of each extinction coefficient to $A(\lambda)$ and are closely related to the concentrations C_{HbO} and C_{HbR}, respectively. The regression coefficient α_0 is expressed as

$$\alpha_0 = \bar{A} - \bar{\varepsilon}_{\mathrm{HbO}}\alpha_{\mathrm{HbO}} - \bar{\varepsilon}_{\mathrm{HbR}}\alpha_{\mathrm{HbR}}, \tag{17}$$

where $\bar{A}$, $\bar{\varepsilon}_{\mathrm{HbO}}$, and $\bar{\varepsilon}_{\mathrm{HbR}}$ are the averages of $A(\lambda)$, $\varepsilon_{\mathrm{HbO}}(\lambda)$, and $\varepsilon_{\mathrm{HbR}}(\lambda)$, respectively, over the wavelength range, and α_0

represents the bias component of $A(\lambda)$. Thus, a_0 describes the degree of contribution of the attenuation due to light scattering in the brain to the absorbance spectrum $A(\lambda)$ and so is related to the coefficient a and the exponent b in Eq. (15). At the same time, α_0 is also affected by the absorption coefficient of the brain, since $A(\lambda)$ is generally a function of the tissue absorption coefficient and the reduced scattering coefficient.

In order to investigate the relationship between the regression coefficients and the values of C_{HbO}, C_{HbR}, a, and b, we performed MCS for the diffuse reflectance from the rat cortical tissue through the skull at $\lambda = 500$, 520, 540, 560, 570, 580, 600, 730, and 760 nm using various values of C_{HbO}, C_{HbR}, a, and b. We used the MCS source code developed by Wang et al.,[5] in which the Henyey-Greenstein phase function is applied to the sampling of the scattering angle of photons. The simulation model consisted of a single layer representing cortical tissue. In a single simulation of diffuse reflectance at each wavelength, 5,000,000 photons were randomly launched. The absorption coefficients of oxygenated hemoglobin $\mu_{a,\mathrm{HbO}}(\lambda)$ and deoxygenated hemoglobin $\mu_{a,\mathrm{HbR}}(\lambda)$ were obtained from the values of $\varepsilon_{\mathrm{HbO}}(\lambda)$ and $\varepsilon_{\mathrm{HbR}}(\lambda)$ in the literature,[39] where the hemoglobin concentration of blood with a 44% hematocrit is 2326 μM of hemoglobin. For the reduced scattering coefficients, the values of a were 60,258, 80,344, 100,430, 120,516, and 180,774 in the simulation, which were derived by multiplying the typical value[40] of a by 0.5, 0.75, 1.0, 1.25, and 1.5, respectively. The values of b were 1.2442, 1.31332, 1.3824, 1.45156, and 1.52068, which were derived by multiplying the typical value[40] of b by 0.5, 0.75, 1.0, 1.25, and 1.5, respectively. The reduced scattering coefficients $\mu_s'(\lambda)$ of the cortical tissue were obtained from Eq. (15). The sum of the absorption coefficients of oxyhemoglobin and deoxyhemoglobin, $\mu_{a,\mathrm{HbO}}(\lambda)$ and $\mu_{a,\mathrm{HbR}}(\lambda)$, represents the absorption coefficient of total hemoglobin $\mu_{a,\mathrm{HbT}}(\lambda)$. The values for $C_{\mathrm{HbT}} = 4.652$, 23.26, and 116.3 μM were used as input to the cortical tissue in the MCS. Tissue oxygen saturation was assumed to be $\mathrm{StO}_2 = 60\%$ for all combinations. For all simulations, the refractive index of the cortical tissue n_c was fixed at 1.4. The thickness of the cortical tissue in each case was set to 5.0 mm.

Figures 2(a) and 2(b) show the values of α_{HbO} and α_{HbR} versus the volume concentrations of oxyhemoglobin C_{HbO} and deoxyhemoglobin C_{HbR}, respectively, for various values of a, as obtained from the MCS. Figures 2(c) and 2(d) show the values of α_{HbO} and α_{HbR} versus the volume concentrations of oxyhemoglobin C_{HbO} and deoxyhemoglobin C_{HbR}, respectively, for various values of b, as obtained from the MCS. In both Figs. 2(a) and 2(c), the value of α_{HbO} increases with the increase of C_{HbO}. Moreover, the value of α_{HbO} changes with the increase

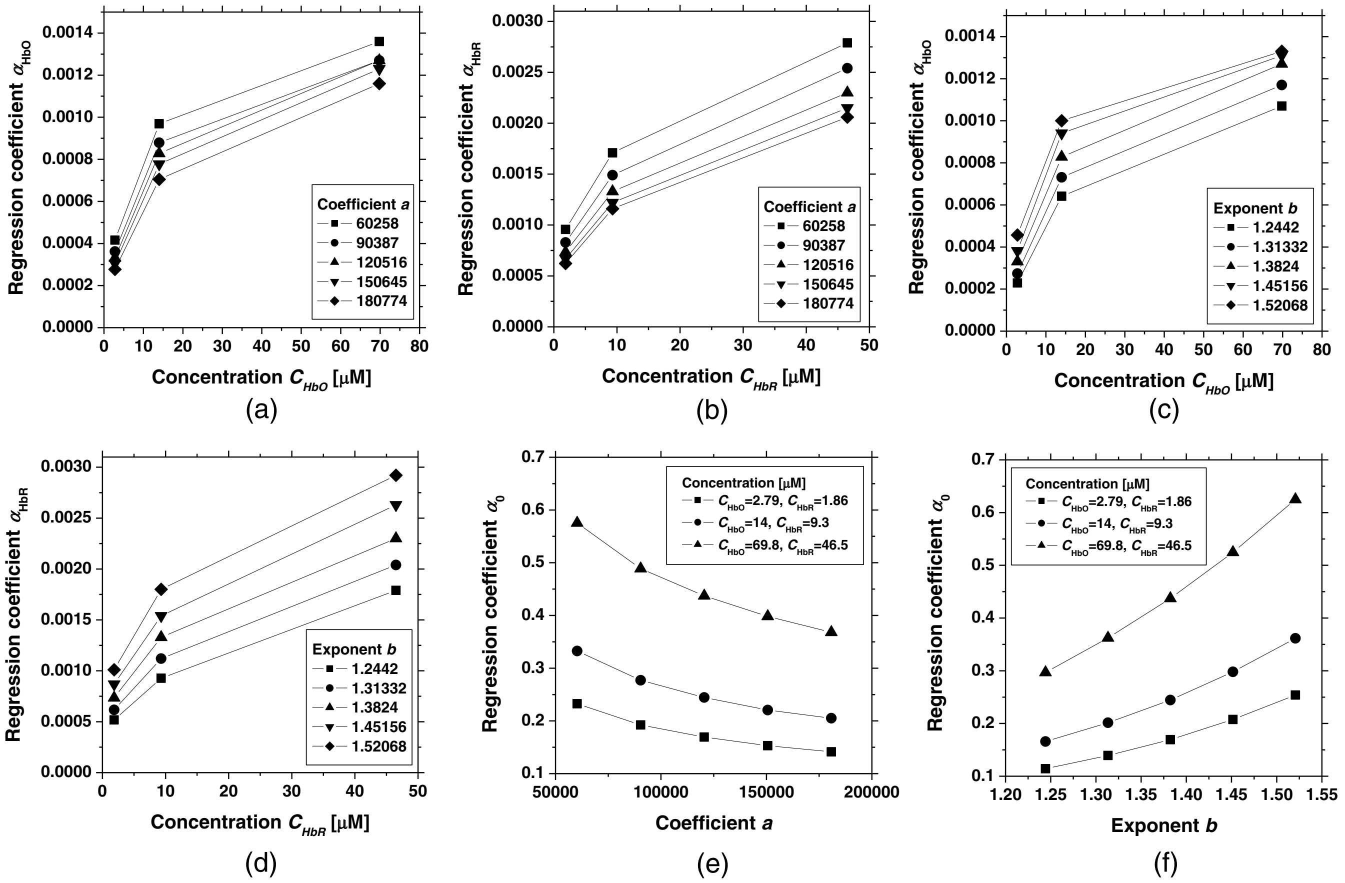

Fig. 2 Regression coefficients versus concentrations of oxygenated hemoglobin C_{HbO} and deoxygenated hemoglobin C_{HbO}, coefficient a, and exponent b, obtained from the Monte Carlo simulations. (a) Regression coefficient α_{HbO} versus concentration C_{HbO} for various values of a. (b) Regression coefficient α_{HbR} versus concentration C_{HbR} for various values of a. (c) Regression coefficient α_{HbR} versus concentration C_{HbO} for various values of b. (d) Regression coefficient α_{HbR} versus concentration C_{HbR} for various values of b. (e) Regression coefficient α_0 versus coefficient a for various values of C_{HbO} and C_{HbR}. (f) Regression coefficient α_0 versus exponent b for various values of C_{HbO} and C_{HbR}.

in the values of a and b. The same tendency can be seen for α_{HbR}, as shown in Figs. 2(b) and 2(d). Figures 2(e) and 2(f) show the values of α_0 versus the values of a and b, respectively, for various values of C_{HbO} and C_{HbR}. The value of α_0 decreases with the increase in the value of a. Moreover, the value of α_0 increases with the increases in C_{HbO} and C_{HbR}. On the other hand, the value of α_0 increases with the increase in the value of b. Therefore, the regression coefficients α_{HbO}, α_{HbR}, and α_0 are related to the volume concentration of oxyhemoglobin C_{HbO}, that of deoxyhemoglobin C_{HbR}, the coefficient a, and the exponent b, respectively. However, C_{HbO}, C_{HbR}, a, and b are not determined by a unique regression coefficient when using only MRA1.

Thus, we conducted further multiple regression analyses to estimate the values of C_{HbO}, C_{HbR}, a, and b based on the combination of regression coefficients α_{HbO}, α_{HbR}, and α_0 that were obtained from MRA1. In this analysis, C_{HbO}, C_{HbR}, and b were regarded as response variables, and the three regression coefficients α_{HbO}, α_{HbR}, and α_0 in Eq. (16) were regarded as predictor variables to determine the regression equations for C_{HbO}, C_{HbR}, and b. The regression equations for C_{HbO}, C_{HbR}, and b are written as

$$C_{\mathrm{HbO}} = \boldsymbol{\beta}_{\mathrm{HbO}} \cdot \boldsymbol{\alpha}_1, \tag{18}$$

$$C_{\mathrm{HbR}} = \boldsymbol{\beta}_{\mathrm{HbR}} \cdot \boldsymbol{\alpha}_1, \tag{19}$$

$$b = \boldsymbol{\beta}_b \cdot \boldsymbol{\alpha}_1, \tag{20}$$

$$\boldsymbol{\alpha}_1 = [1, \alpha_{\mathrm{HbO}}, \alpha_{\mathrm{HbR}}, \alpha_0]^{\mathrm{T}}, \tag{21}$$

$$\boldsymbol{\beta}_{\mathrm{HbO}} = [\beta_{\mathrm{HbO},0}, \beta_{\mathrm{HbO},1}, \beta_{\mathrm{HbO},2}, \beta_{\mathrm{HbO},3}], \tag{22}$$

$$\boldsymbol{\beta}_{\mathrm{HbR}} = [\beta_{\mathrm{HbR},0}, \beta_{\mathrm{HbR},1}, \beta_{\mathrm{HbR},2}, \beta_{\mathrm{HbR},3}], \tag{23}$$

$$\boldsymbol{\beta}_b = [\beta_{b,0}, \beta_{b,1}, \beta_{b,2}, \beta_{b,3}]. \tag{24}$$

The symbol $[\,]^{\mathrm{T}}$ represents the transposition of a vector. We refer to this analysis as MRA2. On the other hand, in the preliminary investigation, we found that adding b to the predictor variables can improve the accuracy of the estimation of a. Therefore, b, α_{HbO}, α_{HbR}, and α_0 are regarded as the predictor variables, and the given values of a are regarded as the response variables for determining the regression equation for a, which is written as

$$a = \boldsymbol{\beta}_a \cdot \boldsymbol{\alpha}_2, \tag{25}$$

where

$$\boldsymbol{\alpha}_2 = [1, \alpha_{\mathrm{HbO}}, \alpha_{\mathrm{HbR}}, \alpha_0, b]^{\mathrm{T}}, \tag{26}$$

$$\boldsymbol{\beta}_a = [\beta_{a,0}, \beta_{a,1}, \beta_{a,2}, \beta_{a,3}\beta_{a,4}]. \tag{27}$$

We refer to this analysis as MRA3. The coefficients $\beta_{\mathrm{HbO},j}$, $\beta_{\mathrm{HbR},j}$, $\beta_{b,j}$, $(j = 0,\ 1,\ 2,\ 3)$, and $\beta_{a,k}$ $(k = 0,\ 1,\ 2,\ 3,\ 4)$ are unknown and must be determined before estimating C_{HbO}, C_{HbR}, b, and a.

We used MCS as the foundation to determine reliable values of $\beta_{\mathrm{HbO},j}$, $\beta_{\mathrm{HbR},j}$, $\beta_{b,j}$, and $\beta_{a,k}$. The simulation model used here consisted of a single layer of cortical tissue, in which $\mu_a(\lambda)$ and $\mu_s'(\lambda)$ are homogeneously distributed. The absorption coefficients $\mu_a(\lambda)$ converted from the concentrations C_{HbO} and C_{HbR} and the reduced scattering coefficient $\mu_s'(\lambda)$ deduced by the coefficient a and the exponent b were provided as inputs to the simulation, whereas the diffuse reflectance spectrum $r(\lambda)$ was derived as output. The input values of C_{HbO}, C_{HbR}, a, and b and the output reflectance spectra are useful as the data set in statistically determining the values of $\beta_{\mathrm{HbO},i}$, $\beta_{\mathrm{HbR},i}$, $\beta_{b,i}$, and $\beta_{a,j}$ for determining the absolute values of C_{HbO}, C_{HbR}, a, and b. The five different values of 60,258, 80,344, 100,430, 120,516, and 180,774 were calculated by multiplying the typical value[40] of a by 0.5, 0.75, 1.0, 1.25, and 1.5, respectively, whereas the five values of 1.2442, 1.31332, 1.3824, 1.45156, and 1.52068 were calculated by multiplying the typical value[40] of b by 0.5, 0.75, 1.0, 1.25, and 1.5, respectively. The reduced scattering coefficients $\mu_s'(\lambda)$ of the cortical tissue with the 25 different values were derived using Eq. (15). The sum of the absorption coefficients of oxyhemoglobin and deoxyhemoglobin $\mu_{a,\mathrm{HbO}}(\lambda) + \mu_{a,\mathrm{HbR}}(\lambda) = \mu_{a,\mathrm{HbT}}(\lambda)$ for $C_{\mathrm{HbT}} = 4.652$, 23.26, and 116.3 μM was used as input to the cortical tissue in the simulation. Tissue oxygen saturation StO_2 was determined by $\mu_{a,\mathrm{HbO}}(\lambda)/\mu_{a,\mathrm{HbT}}(\lambda)$, and values of 0%, 20%, 40%, 60%, 80%, and 100% were used for the simulation. The above values were also used for the refractive index of the cortical layer. In total, 450 diffuse-reflectance spectra at $\lambda = 500$, 520, 540, 560, 570, 580, 600, 730, and 760 nm were simulated under the various combinations of C_{HbO}, C_{HbR}, a, and b. The MRA1 analysis for each simulated spectrum based on Eq. (16) generated the 450 sets of vector α_1 and concentrations C_{HbO} and C_{HbR} and exponent b, and the 450 sets of vector α_2 and coefficient a. The coefficient vectors β_{HbO}, β_{HbR}, and β_b were statistically determined by performing MRA2, whereas the coefficient vector β_{HbO} was determined statistically by performing MRA3. Once β_{HbO}, β_{HbR}, β_b, and β_a were obtained, C_{HbO}, C_{HbR}, a, and b were calculated from α_{HbO}, α_{HbR}, and α_0, which were derived from MRA1 for the measured reflectance spectrum, without the MCS, as shown in Fig. 1(b). Therefore, the spectrum of the reduced scattering coefficient $\mu_s'(\lambda)$ and that of the absorption coefficient $\mu_a(\lambda)$ were reconstructed by Eqs. (12) and (15), respectively, from the measured reflectance spectrum.

3 Experiments

3.1 *Imaging System*

Figure 3(a) shows a schematic diagram of the experimental system used in the present study. A white-light emitting diode (LED) (LA-HDF158A, Hayashi Watch Works Co., Ltd., Tokyo, Japan) illuminated the surface of the exposed cortex via a light guide and a ring-shaped illuminator with a polarizer. The light source covered a range from 400 to 780 nm. Diffusely reflected light was received by a 24-bit RGB CCD camera (DFK-31BF03.H, Imaging Source LLC, Charlotte, NC, USA) without an IR cut filter via an analyzer and a camera lens to acquire an RGB image of 640 × 480 pixels. The primary polarization plate (ring-shaped polarizer) and the secondary polarization plate (analyzer) were placed in a crossed Nicols alignment in order to reduce specular reflection from the sample surface. A standard white diffuser was used to regulate the white balance of

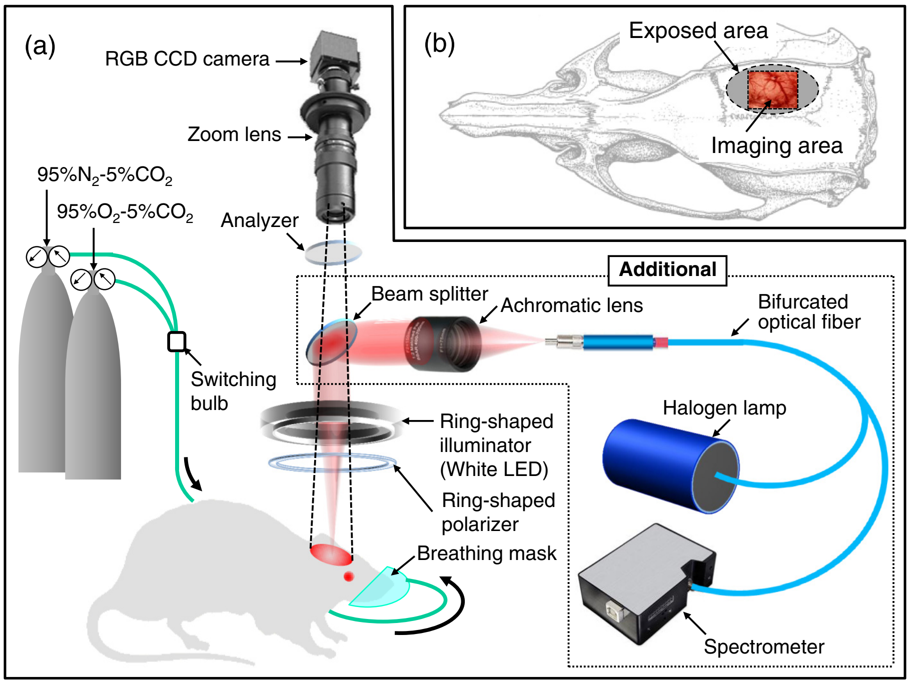

Fig. 3 (a) Schematic diagram of the experimental system and (b) representation of the rat skull with an RGB image of the exposed rat brain.

the camera. In order to evaluate the accuracy of the WEM, the reflectance spectra of cortex were simultaneously measured by a fiber-coupled spectrometer (USB4000-XRS-ES, Ocean Optics Inc., Dunedin, Florida, USA) for an integration time of 130 ms as reference data. Before the measurements of RGB images and reflectance spectra, the area measured using the spectrometer was confirmed by projecting light from a halogen lamp (HL-2000, Ocean Optics Inc.) onto the surface of the cortex via one lead of a bifurcated fiber, a lens, and a beam splitter. The RGB image of the sample, including the spot of light illuminated by the halogen lamp, was stored in the PC, and the size and coordinates of the spot were then specified as the area measured by the spectrometer. After the halogen lamp was turned off, the measurements of RGB images and reflectance spectra were performed simultaneously. Using the WEM, reflectance images ranging from 500 to 760 nm at intervals of 10 nm were reconstructed from an RGB image acquired at an exposure time of 65 ms. This means that the spectral reflectance images at 27 wavelengths can be obtained with a temporal resolution of 15 fps. The field of view of the system was $9.31 \times 6.98\ \mathrm{mm}^2$ with 1024×768 pixels. The lateral resolution of the images was estimated to be 9.1 μm. The multispectral reflectance images with 400×400 pixels at nine wavelengths (500, 520, 540, 560, 570, 580, 600, 730, and 760 nm) were then used to estimate the images of C_{HbO}, C_{HbR}, a, b, $\mu_a(\lambda)$, and $\mu_s'(\lambda)$ according to the process described in Fig. 1.

3.2 *Phantom Experiments*

To confirm the validity of the proposed method, we performed experiments using tissue-like optical phantoms. We prepared agar solution by diluting agarose powder (Fast Gene AG01; NIPPON Genetics EUROPE GmbH, Düren, NRW, Germany) with saline at a weight ratio of 1.0%. To simulate the scattering condition, a mixture of polystyrene latex beads solution with a 0.1-μm mean particle size (LB1-15L; Sigma-Aldrich Japan K. K. Tokyo, Japan) and that with a 1.1-μm mean particle size (LB11-15L; Sigma-Aldrich Japan K. K.) was added to the agarose solution. The resultant solution was used as the base material. The volume concentration of the polystyrene solutions ranged from 2.75% to 11.0%. An optical phantom layer was made by adding a small amount of fully oxygenated hemoglobin extracted from horse blood to the base material. All phantoms were hardened in molds having the required thickness and size by being cooled at approximately 5.5°C for 30 min. The thickness of each phantom was 0.5 cm, while the area of each phantom was $2.6 \times 4.5\ \mathrm{cm}^2$. In the preliminary experiments, we attempted to measure the phantoms with hemoglobin deoxygenated by $Na_2S_2O_4$ solution. However, the measured diffuse reflectance spectra had a tendency to exhibit unexpected fluctuation and it was difficult to maintain the stable condition of the deoxygenated spectra during the experiments. To avoid the potential uncertainty of the estimation of the total hemoglobin with the condition of $\mathrm{StO}_2 = 0\%$, the phantoms with hemoglobin deoxygenated by $Na_2S_2O_4$ solution were excluded from the measurements in this study. We made 22 optical phantoms with different combinations of C_{HbO}, C_{HbR}, a, and b.

As preparatory measurements, we first determined the absorption coefficient μ_a and reduced scattering coefficients μ_s' of each phantom at 500, 520, 540, 560, 570, 580, 600, 730, and 760 nm, because they are necessary for the MCS to deduce the empirical formula for C_{HbO}, C_{HbR}, a, and b. The spectra of the absorption coefficient $\mu_a(\lambda)$ and reduced scattering coefficients $\mu_s'(\lambda)$ are also required to calculate the given values for C_{HbO}, C_{HbR}, a, and b. For this purpose, we measured the diffuse reflectance and total transmittance spectra of each phantom individually. A 150-W halogen-lamp light source (LA-150SAE; Hayashi Watch Works Co., Ltd.) illuminated the phantom via a light guide (LGC1-5L1000; Hayashi Watch Works Co., Ltd.) and lens with a spot diameter of

0.2 cm. The diameter and focal length of the lens are 5.0 and 10 cm, respectively. The thickness of each phantom in the preparatory measurements was 0.1 cm, while the area of each phantom was $2.6 \times 4.5\ \mathrm{cm}^2$. The phantom was placed between two glass slides having a thickness of 0.1 cm and fixed at the sample holder of an integrating sphere (RT-060-SF, Labsphere Incorporated). The detected area of the phantom was circular with a diameter of 2.2 cm. Light diffusely reflected from the detected area was received at the input face of an optical fiber probe having a diameter of 400 μm which was placed at the detector port of the sphere. The fiber transmits the received light into a multichannel spectrometer (USB2000, Ocean Optics Inc.), which measured reflectance or transmittance spectra in the visible to near-infrared wavelength region under the control of a personal computer.

To determine $\mu_a(\lambda)$ and $\mu_s'(\lambda)$ from the measured diffuse reflectance and total transmittance spectra, we utilized the inverse Monte Carlo method (IMC).[41] In the IMC, the MCS of the reflectance and transmittance spectra were iterated for different values of $\mu_a(\lambda)$ and $\mu_s'(\lambda)$ until the difference between the simulated and measured spectral values decreased below a predetermined threshold. The values used in the last step of the iteration were adopted as the final results. This process was carried out at 500, 520, 540, 560, 570, 580, 600, 730, and 760 nm, and wavelength-dependent properties of $\mu_a(\lambda)$ and $\mu_s'(\lambda)$ were obtained for each phantom. In these calculations, the refractive index was assumed to be 1.33 for all phantoms in the whole wavelength range. The concentrations of oxygenated hemoglobin C_{HbO} and deoxygenated hemoglobin C_{HbR} in each phantom were calculated from Eq. (12) with the estimated absorption coefficient $\mu_a(\lambda)$ and the known values of $\varepsilon_{\mathrm{HbO}}(\lambda)$ and $\varepsilon_{\mathrm{HbR}}(\lambda)$. The concentration of total hemoglobin C_{HbT} and the tissue oxygen saturation StO_2 in each phantom was calculated from Eqs. (13) and (14), respectively. The coefficient a and the exponent b for each phantom were calculated from the estimated $\mu_s'(\lambda)$ based on Eq. (15). Those values of μ_a, C_{HbO}, C_{HbR}, C_{HbT}, StO_2, μ_s', a, and b obtained by IMC are used as the given values to evaluate the validity of the proposed method experimentally.

We also need to have the conversion vectors for the phantoms used in this study. We generated diffuse reflectance spectra at 500, 520, 540, 560, 570, 580, 600, 730, and 760 nm using the MCS with the conditions of the phantoms. For this simulation, the values of μ_a and μ_s' at 500, 520, 540, 560, 570, 580, 600, 730, and 760 nm were set to be the same as those estimated by IMC. Performing MRA1, MRA2, and MRA3 as described in Sec. 2, we derived the conversion vectors and the corresponding empirical formula for estimating the volume concentrations of oxygenated hemoglobin C_{HbO}, that of deoxygenated hemoglobin C_{HbR}, the coefficient a, and the exponent b.

3.3 *Animal Experiments*

Animal care and experimental procedures were approved by the Animal Research Committee of Tokyo University of Agriculture and Technology. Intraperitoneal anesthesia was implemented with α-chloralose (50 mg/kg) and urethane (600 mg/kg) in five adult male Wister rats (134 to 426 g). Anesthesia was maintained at a depth such that the rat had no response to toe pinch. The rat head was placed in a stereotaxic frame. A longitudinal incision of ~20 mm in length was made along the head midline. The skull bone overlying the parietal cortex was removed with a high-speed drill to form an ellipsoidal cranial window, as shown in Fig. 3(b). In order to confirm the change in reflectance spectra of exposed rat brain, we performed the measurements during normoxia ($t = 0$ to 5 min), hyperoxia ($t = 5$ to 10 min), and anoxia ($t = 10$ to 30 min) by varying FiO_2. Hyperoxia ($\mathrm{FiO}_2 = 95\%$) was induced by $95\%\mathrm{O}_2$–$5\%\mathrm{CO}_2$ gas inhalation, for which a breath mask was used under spontaneous respiration, whereas anoxia ($\mathrm{FiO}_2 = 0\%$) was induced by $95\%\mathrm{N}_2$–$5\%\mathrm{CO}_2$ gas inhalation. In order to identify the respiration arrest (RA), the respiration of the rat was confirmed by observing the periodical movement of the lateral region of the abdomen during the experiments.

In order to evaluate the magnitude of signal S induced by hyperoxia and anoxia, we calculated the change in the signal based on the time series data. The signal at the onset of measurement was selected as a control S_c, which was subtracted from each of the subsequent signals S in the series. Each subtracted value, which demonstrated the change in the signal, $S - S_c$, over time, was normalized by dividing by S_c. The change in the signal is expressed as $\Delta S = \{(S - S_c)/S_c\} \times 100$. The above calculation was applied to the time series of C_{HbO}, C_{HbR}, C_{HbT}, StO_2, a, b, and $\mu_s'(\lambda)$. The time of RA can differ from sample to sample. Therefore, we divided the time course of the estimated value during anoxia into two periods: anoxia 1 and anoxia 2. Anoxia 1 is the period between the onset of anoxia and RA, whereas anoxia 2 is the period between RA and the end of the measurement. The time averages of the estimated values over the periods of normoxia, hyperoxia, anoxia 1, and anoxia 2 were then calculated and averaged over all five samples.

3.4 *Statistical Considerations*

A region of interest (ROI) of 40×40 pixels was placed in an image for each resultant image. An unpaired Student's t-test was used for statistical analysis when comparing the *in vivo* results of the normoxic condition with those for the hyperoxic condition or with those for the anoxic conditions. The normality of the averaged value over the seven samples for each condition was tested using a Shapiro-Wilk test before the Student's t-test. A P value of <0.05 was considered to be statistically significant.

4 Results and Discussion

Figure 4 shows the comparisons between the estimated and given values for (a) oxygenated hemoglobin C_{HbO}, (b) deoxygenated hemoglobin C_{HbR}, (c) total hemoglobin C_{HbT}, (d) tissue oxygen saturation StO_2, (e) coefficient a, and (f) exponent b, obtained from the phantom experiments. In Figs. 4(a), 4(c), 4(e), and 4(f), the estimated values are well correlated with the given values. Correlation coefficients between the estimated and given values are 0.91 ($P < 0.0001$), 0.95 ($P < 0.0001$), 0.84 ($P < 0.0001$) and 0.46 ($P = 0.029$) for C_{HbO}, C_{HbT}, a, and b, respectively. In Figs. 4(b) and 4(d), all estimated values of C_{HbR} and StO_2 are close to 0 μM and 100%, respectively, which is consistent with the fact that the hemoglobin solution used in the phantoms was fully oxygenated hemoglobin, as described above. These results indicate the validity of the proposed method for estimating the volume concentrations C_{HbO} and C_{HbR}, the coefficient a, and the exponent b. Figure 5 shows the comparisons between the estimated and given values for (a) absorption coefficient μ_a and (b) reduced scattering coefficient μ_s'. Reasonable results were obtained for both μ_a and μ_s'. Correlation coefficients between the estimated and given values are 0.97 ($P < 0.0001$) and 0.78 ($P < 0.0001$) for μ_a and μ_s', respectively. These results demonstrate the validity of the

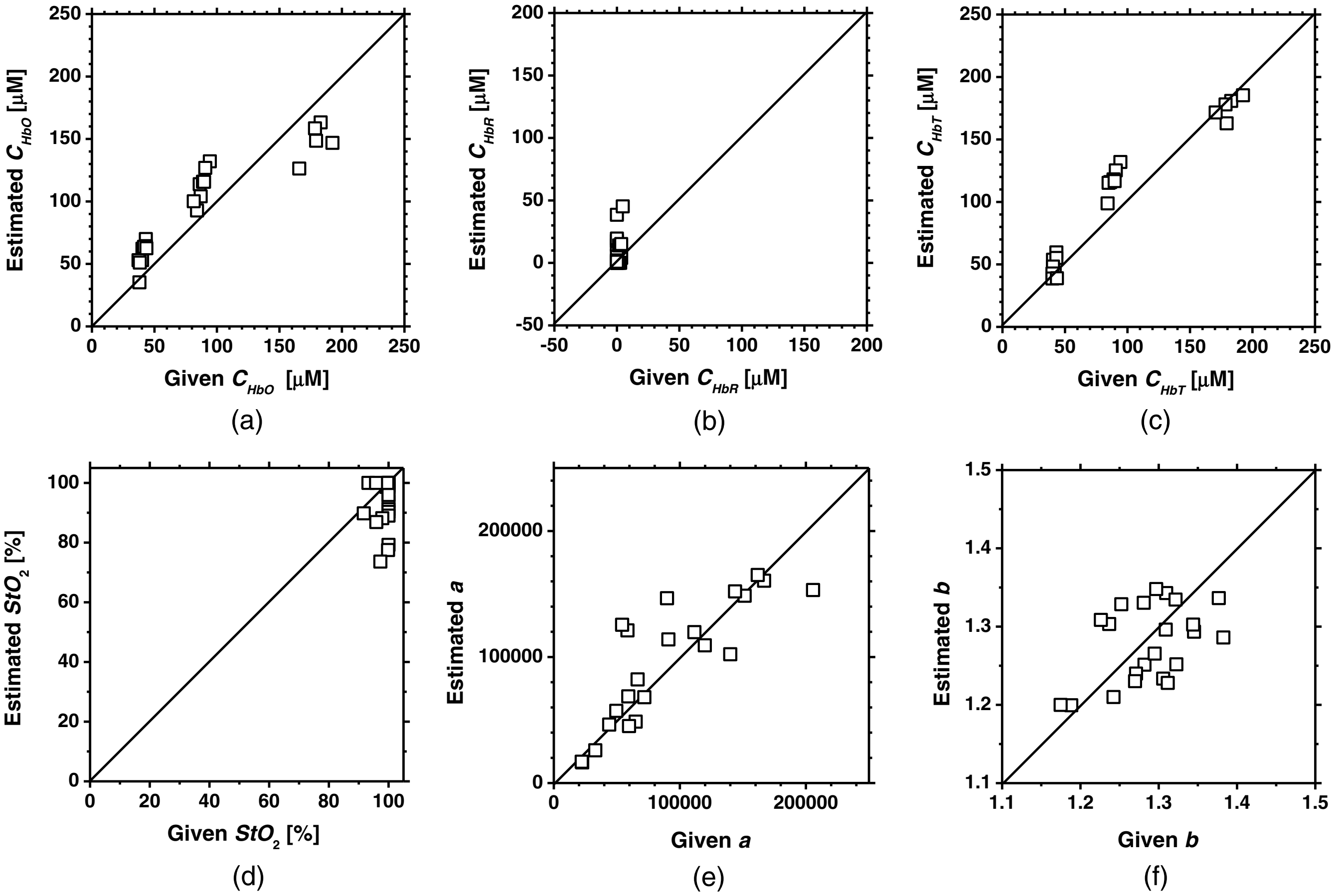

(a) (b) (c)

(d) (e) (f)

Fig. 4 Comparisons between the estimated and given values for (a) oxygenated hemoglobin C_{HbO}, (b) deoxygenated hemoglobin C_{HbR}, (c) total hemoglobin C_{HbT}, (d) tissue oxygen saturation StO_2, (e) coefficient *a*, and (f) exponent *b*, obtained from the phantom experiments.

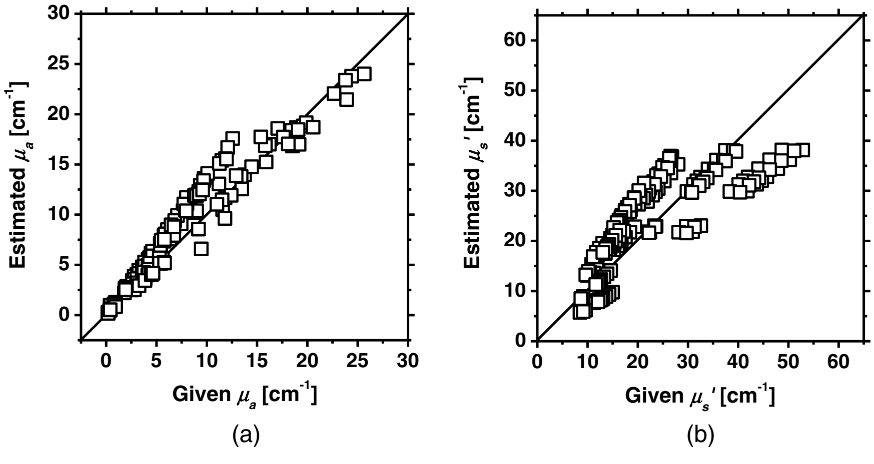

(a) (b)

Fig. 5 Comparisons between the estimated and given values for (a) absorption coefficient μ_a and (b) reduced scattering coefficient μ_s', obtained from the phantom experiments.

proposed method for estimating absorption and reduced scattering coefficients from the diffuse reflectance spectrum.

Figure 6 shows the typical spectral reflectance images at 500, 520, 540, 560, 570, 580, 600, 730, and 760 nm estimated from the RGB image of *in vivo* rat brain under normoxia by the WEM. Spectral reflectance images of the cerebral cortex were successfully reconstructed from the RGB image using the proposed method. The distribution of blood vessels in the cortical tissue can be clearly recognized in the estimated reflectance images at 500, 520, 540, 560, 570, and 580 nm. The images at 600, 730, and 760 nm have low contrast between the parenchyma region and the blood vessel region, which indicates the lower absorption coefficient of hemoglobin at lower wavelengths.

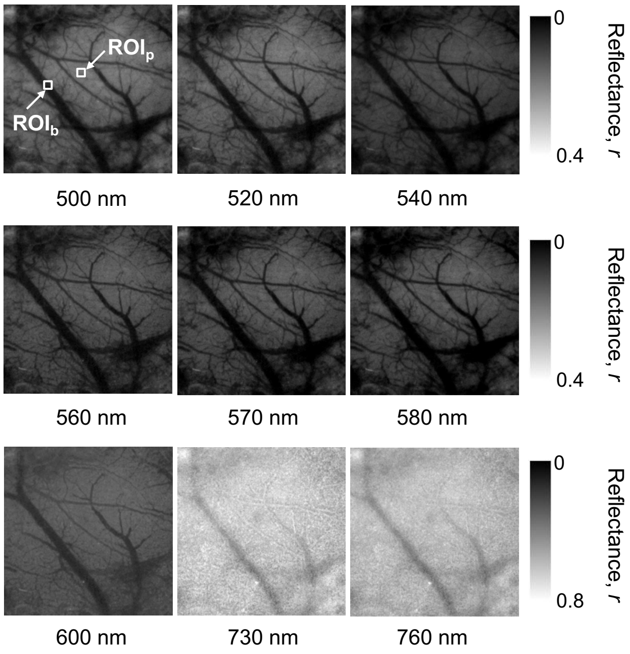

Fig. 6 Typical estimated multispectral images $r(\lambda)$ of the exposed rat brain under normoxia.

Figure 7 shows the reflectance spectra estimated using the WEM and the reflectance spectra measured using the spectrometer for (a) normoxia, (b) hyperoxia, and (c) anoxia immediately after RA. The estimated reflectance spectra for a blood vessel and that for parenchyma in each graph of Fig. 7 is the average values over the $\mathrm{ROI_b}$ and $\mathrm{ROI_p}$, respectively. In this case, both $\mathrm{ROI_b}$ and $\mathrm{ROI_p}$ were selected to be the same as the measured area by the spectrometer. The reflectance spectra estimated using the WEM are comparable to the spectra measured using the spectrometer for the different respiration conditions. The estimated spectra under hyperoxia and anoxia are dominated by the spectral characteristics of oxygenated hemoglobin and deoxygenated hemoglobin, respectively. The values of GFC obtained from five samples summarized in Table 1 in the revised manuscript indicate the accurate spectral reconstruction by WEM.

Figure 8 shows the typical estimated images of exposed rat brain under normoxia obtained using the proposed method for (a) oxygenated hemoglobin C_{HbO}, (b) deoxygenated hemoglobin C_{HbR}, (c) total hemoglobin C_{HbT}, (d) tissue oxygen saturation $\mathrm{StO_2}$, (e) coefficient a, and (f) exponent b. In Figs. 8(a)–8(c), the values of C_{HbO}, C_{HbR}, and C_{HbT}, respectively, in the blood vessel region are higher than those in the parenchyma region, which indicates the difference in blood volume between

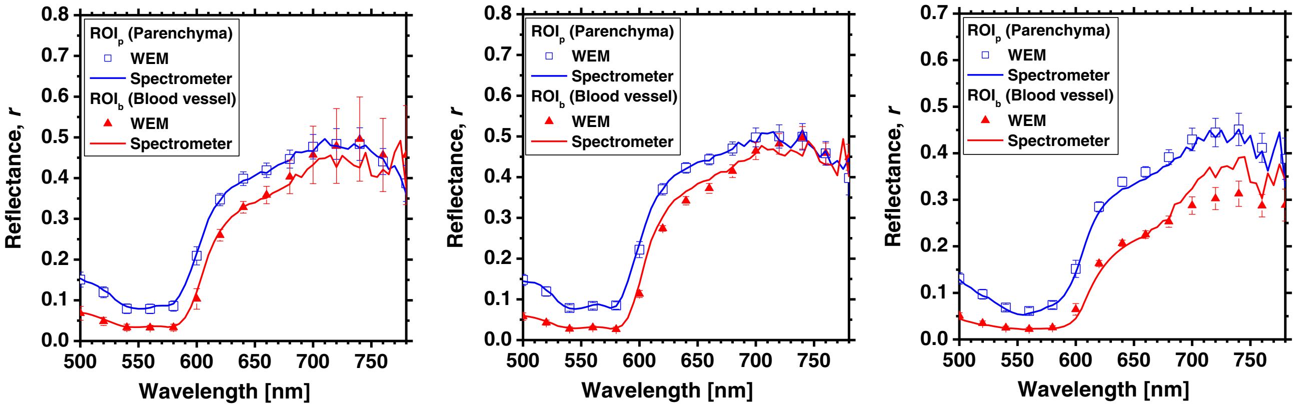

(a) (b) (c)

Fig. 7 Comparison of the estimated reflectance spectra averaged over the ROIs in Fig. 4 (white squares) and the reference spectra measured by spectrometer for (a) normoxia, (b) hyperoxia, and (c) anoxia.

Table 1 The goodness-of-fit coefficient (GFC) obtained from the five samples.

		GFC					
Sample	Region	Mean	±SD	Max	Min	Number of spectra	Accuracy
#1	Parenchyma	0.9992	0.0003	0.9998	0.9980	121	Good
#2	Parenchyma	0.9982	0.0006	0.9992	0.9964	361	Colorimetrically accurate
#3	Parenchyma	0.9975	0.0015	0.9994	0.9947	361	Colorimetrically accurate
#4	Parenchyma	0.9990	0.0005	0.9998	0.9975	361	Good
#5	Parenchyma	0.9997	0.0002	0.9999	0.9985	361	Good
	Blood vessel	0.9984	0.0013	0.9999	0.9935	361	Colorimetrically accurate

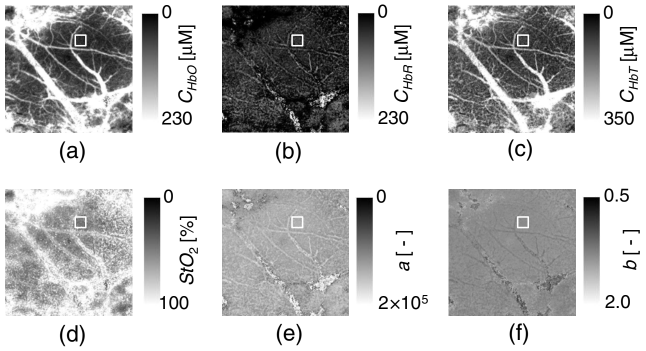

Fig. 8 Estimated images of exposed rat brain obtained using the proposed method under normoxia for (a) oxygenated hemoglobin C_{HbO}, (b) deoxygenated hemoglobin C_{HbR}, (c) total hemoglobin C_{HbT}, (d) tissue oxygen saturation StO_2, (e) coefficient *a*, and (f) exponent *b*.

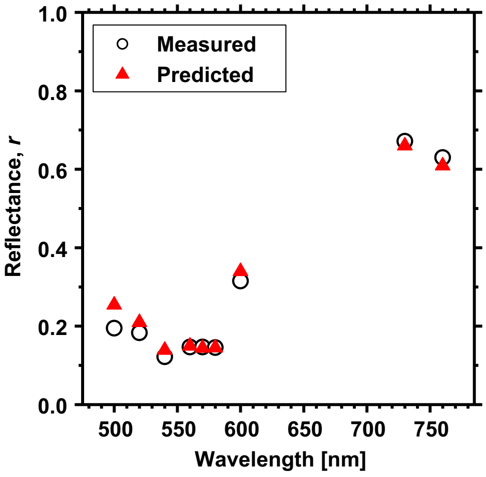

Fig. 11 Comparison between the measured reflectance spectrum and the predicted reflectance spectrum for the μ_a and μ_s', as shown in Fig. 10.

the blood vessels and the parenchyma. The distribution of StO_2 in the blood vessel region in Fig. 8(d) is probably due to the difference between artery and vein. The average values over the entire region were calculated to be $C_{\text{HbO}} = 150.08 \pm 50.61\ \mu\text{M}$, $C_{\text{HbR}} = 40.11 \pm 12.12\ \mu\text{M}$, $C_{\text{HbT}} = 190.19 \pm 52.05\ \mu\text{M}$, $\text{StO}_2 = 75.52 \pm 7.62\%$, $a = 134{,}458 \pm 3{,}634$, and $b = 1.33 \pm 0.02$, whereas those over the ROI on parenchyma (white square in each image of Fig. 8) were calculated to be $C_{\text{HbO}} = 41.16 \pm 3.13\ \mu\text{M}$, $C_{\text{HbR}} = 42.34 \pm 5.51\ \mu\text{M}$, $C_{\text{HbT}} = 83.49 \pm 6.52\ \mu\text{M}$, $\text{StO}_2 = 49.29 \pm 4.19\%$, $a = 136{,}811 \pm 2298$, and $b = 1.32 \pm 0.01$.

Figure 9 shows the reconstructed images of the exposed rat brain for (a) the absorption coefficient spectrum $\mu_a(\lambda)$ and (b) the reduced scattering coefficient spectrum $\mu_s'(\lambda)$ under normoxia. The average values of $\mu_a(\lambda)$ and $\mu_s'(\lambda)$ over the ROIs

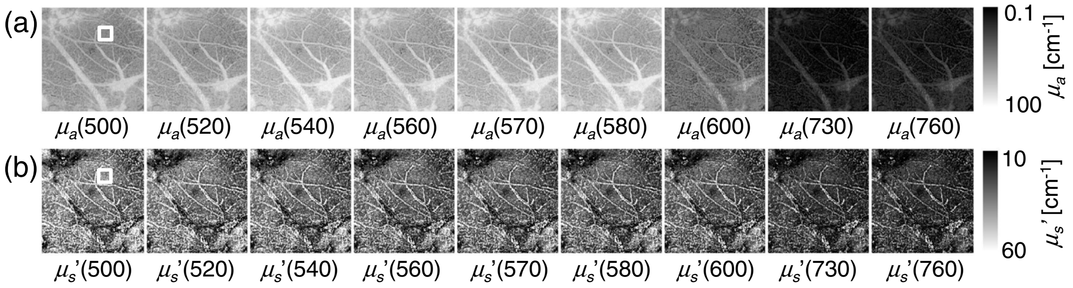

Fig. 9 Typical estimated images of exposed rat brain obtained using the proposed method under normoxia for (a) absorption coefficient $\mu_a(\lambda)$ and (b) reduced scattering coefficient $\mu_s'(\lambda)$.

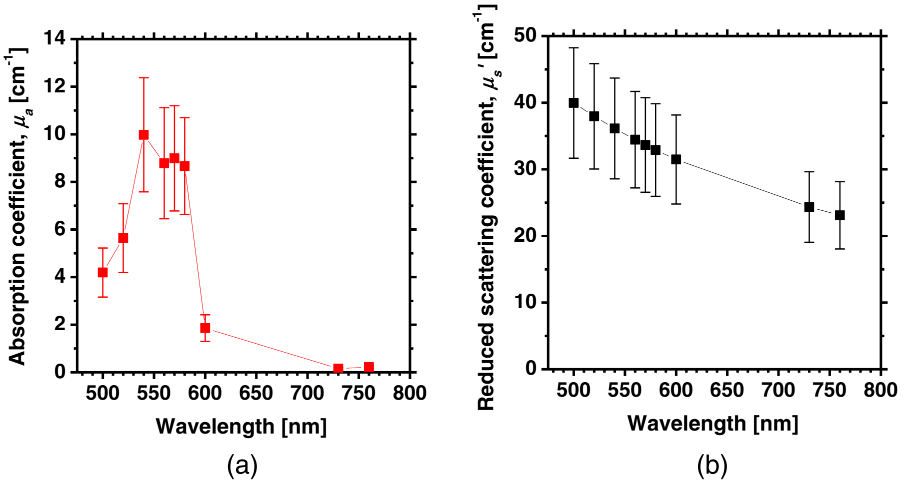

Fig. 10 Estimated spectra averaged over the ROI (white square in Fig. 9) for (a) absorption coefficient $\mu_a(\lambda)$ and (b) reduced scattering coefficient $\mu_s'(\lambda)$. The error bars mean the standard deviations for all pixels in the ROI.

[white squares in Figs. 9(a) and 9(b)] are also shown in Fig. 10. The error bars mean the standard deviations for all pixels in the ROI. The wavelength dependence of $\mu_a(\lambda)$ is dominated by the spectral characteristics of hemoglobin.[39] The reduced scattering coefficients $\mu_s'(\lambda)$ have a broad scattering spectrum, exhibiting a larger magnitude at shorter wavelengths. The spectral features of μ_s' correspond to the typical spectrum of brain tissue published in the literature.[40]

Figure 11 shows the comparison between the measured reflectance spectrum and the predicted reflectance spectrum for the μ_a and μ_s' shown in Fig. 10. The predicted reflectance spectrum is comparable to the measured spectrum. The value of GFC in this case was 0.9974, which shows a good agreement between the measured reflectance spectrum and the predicted reflectance spectrum.

Figure 12 shows the typical *in vivo* results for C_{HbO}, C_{HbR}, C_{HbT}, $\mathrm{StO_2}$, a, and b while varying $\mathrm{FiO_2}$. Figure 13 shows the time courses of change in C_{HbO}, C_{HbR}, C_{HbT}, and $\mathrm{StO_2}$ averaged over the area for the ROI in the parenchyma, as shown in Fig. 12, while varying $\mathrm{FiO_2}$. The values of C_{HbO} and C_{HbR} were increased and decreased, respectively, during hyperoxia, which caused the increase in $\mathrm{StO_2}$. After the onset of anoxia, the values of C_{HbO} and C_{HbR} decreased and increased, respectively. Consequently, the value of $\mathrm{StO_2}$ was dramatically decreased. The value of C_{HbT} begins to increase before RA and reaches a maximum amplitude approximately 1 min after

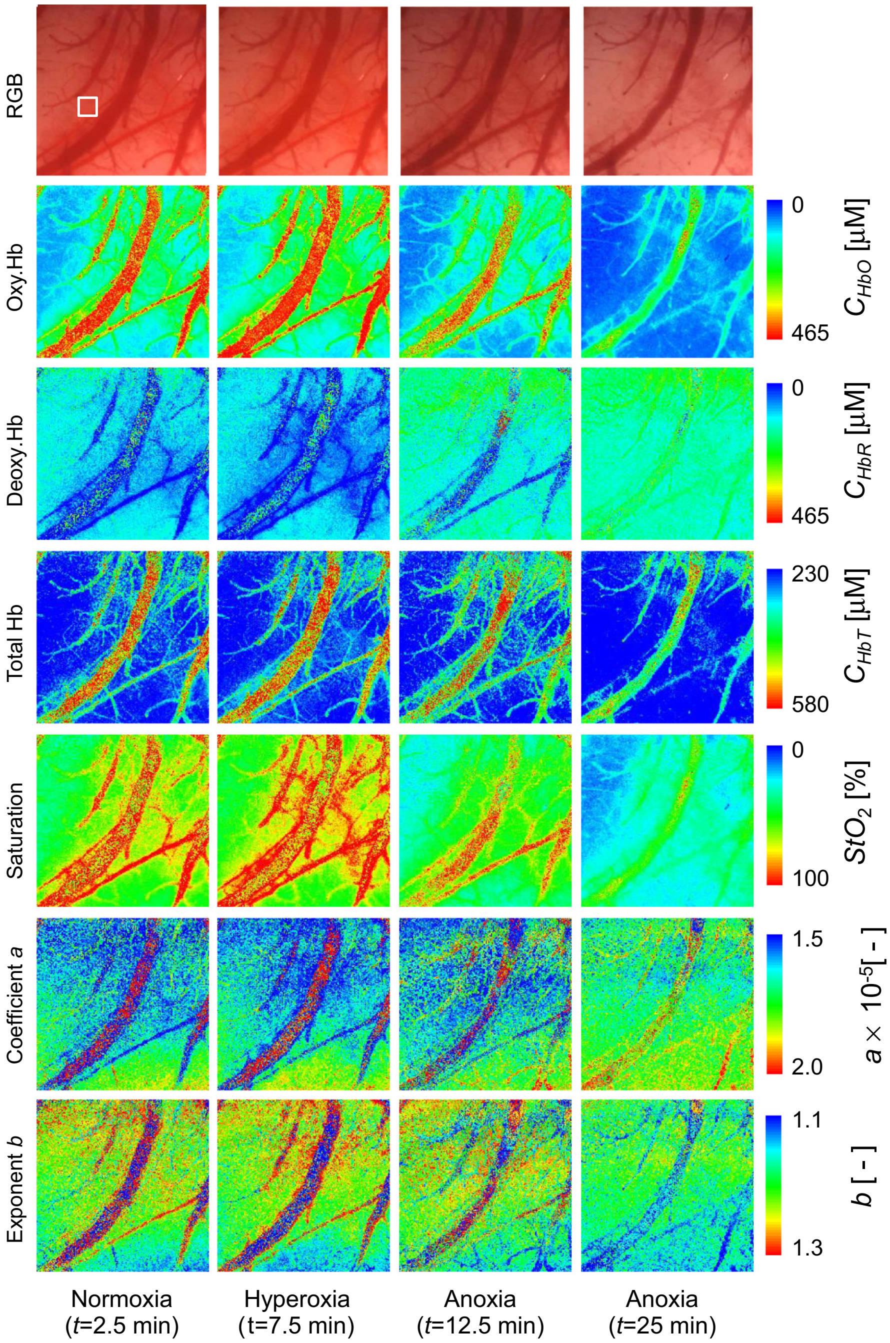

Fig. 12 Typical images for *in vivo* results while varying $\mathrm{FiO_2}$ (from top to bottom: RGB image, C_{HbO}, C_{HbR}, C_{HbT}, $\mathrm{StO_2}$, a, and b).

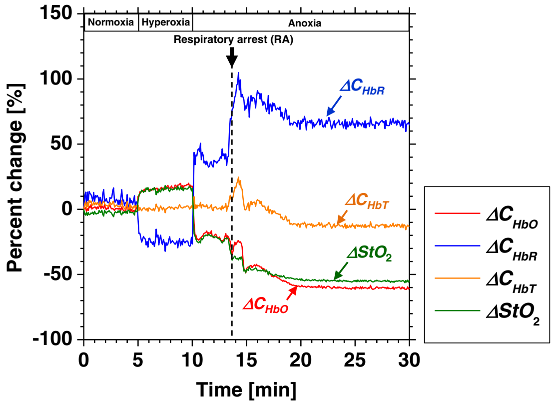

Fig. 13 Time courses of ΔC_{HbO}, ΔC_{HbR}, ΔC_{HbT}, and $\Delta \mathrm{StO}_2$ averaged over the ROI in the parenchyma region shown in Fig. 9 while varying FiO_2.

RA, which is indicative of an increase in blood flow for compensating hypoxia. The period between the onset of anoxia and respiratory arrest averaged over all five samples was 499 ± 207 s. Immediately after RA, the values of both C_{HbO} and C_{HbT} decreased rapidly. The time courses of C_{HbO}, C_{HbR}, C_{HbT}, and StO_2 while varying FiO_2 are consistent with the well-known hemodynamic responses to the change in the fraction of inspired oxygen. Minor fluctuations in both C_{HbO} and C_{HbT} approximately 2.5 min after RA are probably caused by the changes in blood volume due to vasoconstriction and vasodilatation.

Figure 14 shows the time averages over the period of normixia, hyperoxia, anoxia 1 (before RA), and anoxia 2 (after RA) after respiratory arrest for (a) C_{HbO}, (b) C_{HbR}, (c) C_{HbT}, and (d) StO_2 averaged over the ROIs for all five samples. The trends of C_{HbO}, C_{HbR}, C_{HbT}, and StO_2 shown in Figs. 12 and 13 were apparent in all five samples. The average values of StO_2 during normoxia over all five samples were $47.49 \pm 14.42\%$, which is lower than the value of around 60% reported in the literature.[38,42] This may be due to the experimental conditions of the present study, such as the type of anesthetic used, the anesthetic depth, or uncontrolled body temperature.

Figure 15 shows the time courses of coefficient a, exponent b, $\mu_s'(500)$, and $\mu_s'(760)$ averaged over the area corresponding to the ROIs in the parenchyma, as shown in Fig. 12, while varying FiO_2. During the period from the onset of anoxia until RA, coefficient a and exponent b decrease slightly and increase slightly, respectively. The changes in the scattering parameters decrease the reduced scattering coefficient μ_s'. On the other hand, the values of $\mu_s'(500)$ and $\mu_s'(760)$ increased remarkably after RA.

Figure 16 shows the time average over the period of normixia, hyperoxia, anoxia 1, and anoxia 2 for (a) coefficient a, (b) exponent b (c) $\mu_s'(500)$, and (d) $\mu_s'(760)$ averaged over the ROIs for all five samples. The same tendencies of a, b, $\mu_s'(500)$, and $\mu_s'(760)$ shown in Figs. 12 and 15 were applicable to the average values over all five samples. Changes in the reduced scattering coefficients after the onset of N_2-inhalation imply morphological changes in brain tissue. Mitochondrial respiration is inhibited during the ischemia-like condition by the

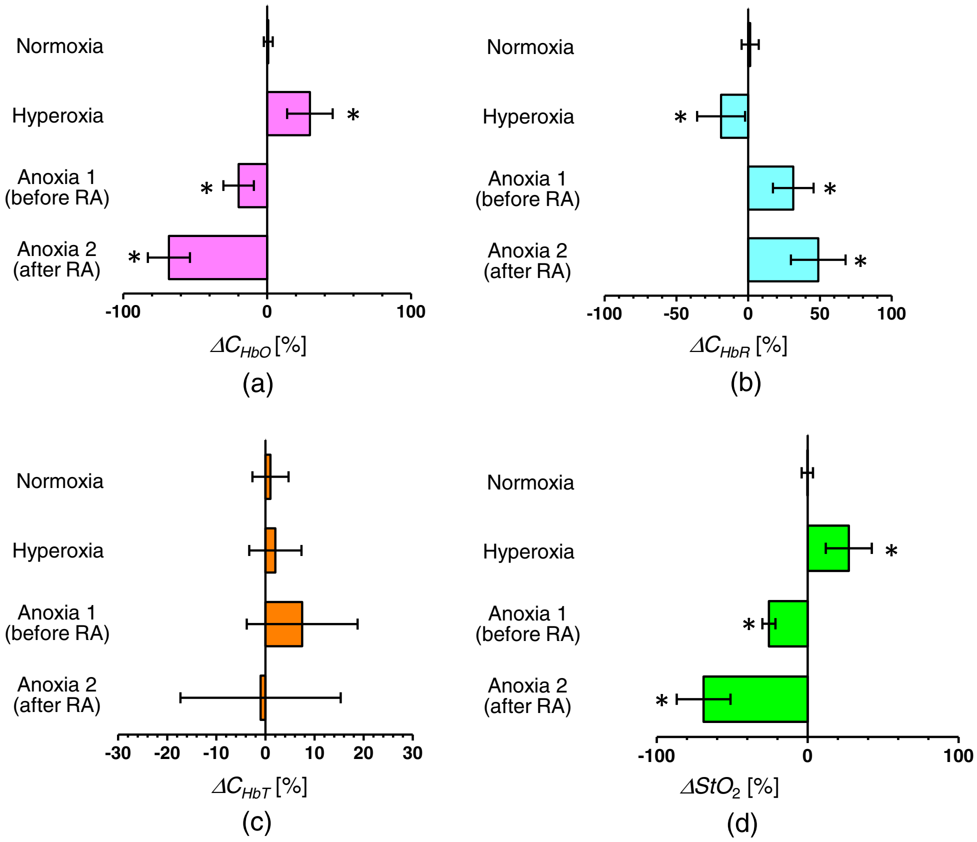

Fig. 14 Time averages over the period of normoxia, hyperoxia, anoxia 1 (before RA), and anoxia 2 (after RA) after respiratory arrest for (a) ΔC_{HbO}, (b) ΔC_{HbR}, (c) ΔC_{HbT}, and (d) $\Delta \mathrm{StO}_2$ averaged over the ROIs for all five samples. The error bars show the standard deviations ($n = 5$). $^*P < 0.05$.

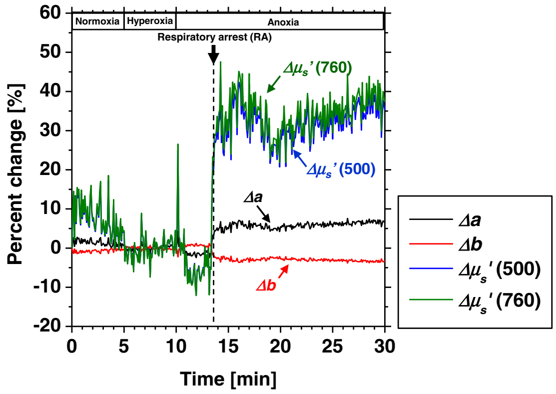

Fig. 15 Time courses of Δa, Δb, $\Delta\mu_s'(500)$, and $\Delta\mu_s'(760)$ averaged over the ROI in the parenchyma region shown in Fig. 9 while varying FiO_2.

rapid drop in O_2 tension, which causes depletion of adenosine triphosphate (ATP). Reduction of ATP production due to the inhibition of mitochondrial respiration leads to failure of the Na^+/K^+ATPase pump.[43] In such a case, extracellular Na^+, Cl^-, and Ca^{2+} rush in, with water following osmotically, causing cell swelling.[44,45] Thus, the slight decreases in μ_s' in Figs. 12, 15, and 16 are most likely caused by cell swelling due to failure of the $Na+/K+$ATPase pump. The remarkable increases in μ_s' after RA are probably caused by the dendritic beading effect, which is indicative of neuronal damage.[44] The necklace-like structure of a large amount of dendritic processes is highly efficient at scattering light, such that bead formation over several minutes reduces the transmitted light intensity.[46–48]

Since the method relying on diffusing reflection integrates all information along the depth direction, the method does not have depth resolution. The depth and diameter of blood vessels usually differ among samples and may change due to the age of the rat. Their correct estimation is essential for precisely estimating the concentrations of oxygenated hemoglobin and deoxygenated hemoglobin for the blood vessel regions. In the present study, we assumed the scattering spectrum of the *in vivo* brain tissue as a power law function. This assumption may be applicable to the parenchyma region with a low volume concentration of blood. However, the diffuse reflectance spectrum from the blood vessel region with a higher volume concentration of blood can be strongly influenced by the scattering properties of the red blood cells (RBCs). It has been reported that RBCs behave as strong scatterers of light, and the reduced scattering coefficient spectrum has a similar wavelength dependence to the absorption spectrum of hemoglobin.[49] Using the empirical formulas obtained from the MCS with an inhomogeneous layer model in which the reduced scattering coefficient spectrum is considered may enable more accurate estimations of the reduced scattering coefficients for the blood vessel regions.

It has been reported that the use of the Lambert-Beer approximation in the analysis of data for ischemia condition in which the values of C_{HbO} and C_{HbR} are dramatically changed provides serious errors.[20] The most serious problem is a large overestimation of the reduction in C_{HbO}, leading to calculated values of C_{HbO} of less than zero. For this problem, they used

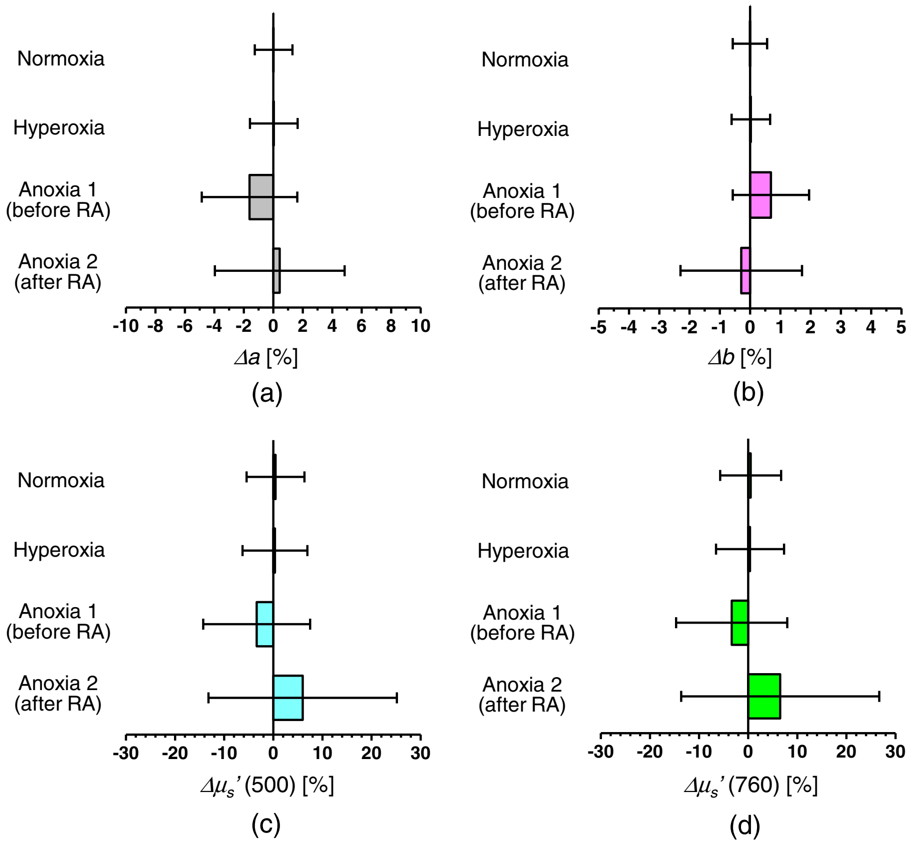

Fig. 16 Time averages over the period of normoxia, hyperoxia, anoxia 1 (before RA), and anoxia 2 (after RA) after respiratory arrest for (a) Δa, (b) Δb, (c) $\Delta\mu_s'(500)$, and (d) $\Delta\mu_s'(760)$ averaged over the ROIs for all five samples. The error bars show the standard deviations ($n = 5$). $^*P < 0.05$.

a nonlinear minimization method to improve the accuracy of the estimations for C_{HbO} and C_{HbR}. We also analyzed the absorbance spectrum based on the Lambert-Beer law for estimating C_{HbO} and C_{HbR}. In this case, the absorbance spectrum was linearly related to C_{HbO} and C_{HbR}. In addition, we used a linear regression model to specify the relationship between the sets of regression coefficients α_{HbO}, α_{HbR}, and α_0 obtained from MRA1 and the values of C_{HbO}, C_{HbR}, a, and b. Therefore, the results obtained by the proposed method may also have some errors in C_{HbO} and C_{HbR} due to the linearization. Although the phantom experiments showed reasonable results for C_{HbO}, C_{HbR}, C_{HbT}, and StO_2, the estimated values of a and b have relative large deviations from the given values, as shown in Fig. 4. Those deviations account for the estimation error in μ_s' shown in Fig. 5(b). The use of α_{HbO}, α_{HbR}, and α_0 and their higher order terms for the vector α_1 and α_2 can extend the current linear empirical formula to the nonlinear regression models. It may be useful to improve the accuracy of the estimations for C_{HbO}, C_{HbR}, a, and b. These issues should be investigated in the future.

5 Conclusions

In summary, a method for imaging reduced scattering coefficients $\mu_s'(\lambda)$ and the absorption coefficients $\mu_a(\lambda)$ of *in vivo* exposed brain tissues based on spectral reflectance images reconstructed from a single snap shot of an RGB image using the WEM was demonstrated in the present report. *In vivo* experiments using exposed rat brain while changing the fraction of inspired oxygen confirmed the feasibility of the proposed method for evaluating both cortical hemodynamics and changes in tissue morphologies due to loss of tissue viability in the brain.

Since the proposed method visualizes both the hemodynamic response and the morphological changes in brain tissue, it may be useful for evaluating brain function and tissue viability in neurosurgery as well as in the diagnosis of several neurological disorders, such as neurotrauma, seizure, stroke, and ischemia. We intend to extend the proposed method in order to investigate brain function in cortical spreading depression and anoxic depolarization.

Acknowledgments

The present study was supported in part by a Grant-in-Aid for Scientific Research from the Japanese Society for the Promotion of Science.

References

1. T. Bonhoeffer and A. Grinvald, *Brain Mapping: The Methods*, Academic Press, San Diego (1996).
2. I. Nishidate, K. Yoshida, and M. Sato, "Changes in optical properties of rat cerebral cortical slices during oxygen glucose deprivation," *Appl. Opt.* **49**(34), 6617–6623 (2010).
3. R. R. Anderson and J. A. Parrish, "The optics of human skin," *J. Invest. Dermatol.* **77**(1), 13–19 (1981).
4. A. Ishimaru, *Wave Propagation and Scattering in Random Media*, Academic Press, New York (1978).
5. L.-H. Wang, S. L. Jacques, and L.-Q. Zheng, "MCML-Monte Carlo modeling of photon transport in multi-layered tissues," *Comput. Methods Programs Biomed.* **47**(2), 131–146 (1995).
6. S. A. Prahl, M. J. C. van Gemert, and A. J. Welch, "Determining the optical properties of turbid media by using the adding-doubling method," *Appl. Opt.* **32**(4), 559–568 (1993).
7. M. S. Patterson, B. Chance, and B. C. Wilson, "Time resolved reflectance and transmittance for the noninvasive measurement of tissue optical properties," *Appl. Opt.* **28**(12), 2331–2336 (1989).
8. J. B. Fishkin et al., "Frequency-domain photon migration measurements of normal and malignant tissue optical properties in a human subject," *Appl. Opt.* **36**(1), 10–20 (1997).
9. T. J. Farrell, M. S. Patterson, and B. Wilson, "A diffusion theory model of spatially resolved, steady-state diffuse reflectance for the noninvasive determination of tissue optical properties in vivo," *Med. Phys.* **19**(4), 879–888 (1992).
10. S. L. Jacques et al., "Video reflectometry to specify optical properties of tissue in vivo," *Proc. SPIE* **IS11**, 211–226 (1993).
11. L. Wang and S. L. Jacques, "Use of a laser beam with an oblique angle on incidence to measure the reduced scattering coefficient of a turbid medium," *Appl. Opt.* **34**(13), 2362–2366 (1995).
12. A. Kienle et al., "Spatially resolved absolute diffuse reflectance measurements for noninvasive determination of the optical scattering and absorption coefficients of biological tissue," *Appl. Opt.* **35**(13), 2304–2314 (1996).
13. S.-P. Lin et al., "Measurement of tissue optical properties by the use of oblique-incidence optical fiber reflectometry," *Appl. Opt.* **36**(1), 136–143 (1997).
14. U. Utzinger and R. R. Richards-Kortum, "Fiber optic probes for biomedical optical spectroscopy," *J. Biomed. Opt.* **8**(1), 121–147 (2003).
15. P. R. Bargo et al., "In vivo determination of optical properties of normal and tumor tissue with white light reflectance and empirical light transport model during endoscopy," *J. Biomed. Opt.* **10**(3), 034018 (2005).
16. N. Rajaram, T. H. Nguyen, and J. W. Tunnell, "Lookup table-based inverse model for determining optical properties of turbid media," *J. Biomed. Opt.* **13**(5), 050501 (2008).
17. B. Yu et al., "Cost-effective diffuse reflectance spectroscopy device for quantifying tissue absorption and scattering in vivo," *J. Biomed. Opt.* **13**(6), 060505 (2008).
18. B. S. Nichols, N. Rajaram, and J. W. Tunnel, "Performance of a lookup table-based approach for measuring tissue optical properties with diffuse optical spectroscopy," *J. Biomed. Opt.* **17**(5), 057001 (2012).
19. R. Hennessy et al., "Monte Carlo lookup table-based inverse model for extracting optical properties from tissue-simulating phantoms using diffuse reflectance spectroscopy," *J. Biomed. Opt.* **18**(3), 037003 (2013).
20. P. B. Jones et al., "Simultaneous multispectral reflectance imaging and laser speckle flowmetry of cerebral blood flow and oxygen metabolism in focal cerebral ischemia," *J. Biomed. Opt.* **13**(4), 044007 (2008).
21. C. Zhou et al., "Diffuse optical correlation tomography of cerebral blood flow during cortical spreading depression in rat brain," *Opt. Express* **14**(3), 1125–1144 (2006).
22. M. B. Bouchard et al., "Ultra-fast multispectral optical imaging of cortical oxygenation, blood flow, and intracellular calcium dynamics," *Opt. Express* **17**(18), 15670–15678 (2009).
23. S. Kawauchi et al., "Diffuse light reflectance signals as potential indicators of loss of viability in brain tissue due to hypoxia: charge-coupled-device-based imaging and fiber-based measurement," *J. Biomed. Opt.* **18**(1), 015003 (2013).
24. C. Yin et al., "Simultaneous detection of hemodynamics, mitochondrial metabolism and light scattering changes during cortical spreading depression in rats based on multi-spectral optical imaging," *NeuroImage* **76**, 70–80 (2013).
25. T. Arnold, M. De Biasio, and R. Leitner, "Hyper-spectral video endoscope for intra-surgery tissue classification using auto-fluorescence and reflectance spectroscopy," *Proc. SPIE*, **8087**, 808711 (2011).
26. A. Basiri et al., "Use of a multi-spectral camera in the characterization of skin wounds," *Opt. Express* **18**(4), 3244–3257 (2010).
27. J. Y. Hardeberg, "Acquisition and Reproduction of Color Images: Colorimetric and Multispectral Approaches," PhD Thesis, Ecole Nationale Superieure des Telecommunications, Paris, France (1999).
28. J. Y. Hardeberg, F. Schmitt, and H. Brettel, "Multispectral color image capture using liquid crystal tunable filter," *Opt. Eng.* **41**(10), 2532–2548 (2002).
29. V. Cheung et al., "Characterization of trichromatic color cameras by using a new multispectral imaging technique," *J. Opt. Soc. Am.* **A22**(7), 1231–1240 (2005).

30. H. L. Shen and J. H. Xin, "Spectral characterization of a color scanner based on optimized adaptive estimation," *J. Opt. Soc. Am. A* **23**(7), 1566–1569 (2006).
31. H. L. Shen, J. H. Xin, and S. J. Shao, "Improved reflectance reconstruction for multispectral imaging by combining different techniques," *Opt. Express* **15**(9), 5531–5536 (2007).
32. F. König, "Reconstruction of natural spectra from color sensor using nonlinear estimation methods," in *IS&T Annual Conference; The Society for Imaging Science and Technology*, pp. 454–457, Cambridge, USA (1997).
33. P. Stigell, K. Miyata, and M. H. Kansari, "Wiener estimation method in estimating of spectral reflectance from RGB image," *Pattern Recogn. Image Anal.* **17**(2), 233–242 (2007).
34. Y. Murakami et al., "Color reproduction from low-SNR multispectral images using spatio-spectral Wiener estimation," *Opt. Express* **16**(6), 4106–4120 (2008).
35. S. Chen and Q. Liu, "Modified Wiener estimation of diffuse reflectance spectra from RGB values by the synthesis of new color for tissue measurements," *J. Biomed. Opt.* **17**(3), 030501 (2012).
36. J. Hernández-Andrés, J. Romero, and R. L. Lee Jr., "Colorimetric and spectroradiometric characteristics of narrow-field-of-view clear skylight in Granada, Spain," *J. Opt. Soc. Am. A* **18**(2), 412–420 (2001).
37. J. R. Mourant et al., "Mechanisms of light scattering from biological cells relevant to noninvasive optical-tissue diagnostics," *Appl. Opt.* **37**(16), 3586–3593 (1998).
38. D. Abookasis et al., "Imaging cortical absorption, scattering, and hemodynamic response during ischemic stroke using spatially modulated near-infrared illumination," *J. Biomed. Opt.* **14**(2), 024033 (2009).
39. S. A. Prahl, *Tabulated Molar Extinction Coefficient for Hemoglobin in Water*, http://omlc.ogi.edu/spectra/hemoglobin/summary.html (18 November 2014).
40. V. Tuchin, *Tissue Optics: Light Scattering Methods and Instruments for Medical Diagnosis*, 2nd ed., SPIE Press, Bellingham, WA (2007).
41. I. Nishidate, Y. Aizu, and H. Mishina, "Estimation of melanin and hemoglobin in skin tissue using multiple regression analysis aided by Monte Carlo simulation," *J. Biomed. Opt.* **9**(4), 700–710 (2004).
42. S. Sato et al., "Real-time optical diagnosis of the rat brain exposed to a laser-induced shock wave: observation of spreading depolarization, vasoconstriction and hypoxemia-oligemia," *PLoS One* **9**(1), e82891 (2014).
43. P. Lipton, "Ischemic cell death in brain neuron," *Physiol. Rev.* **79**(4), 1432–1568 (1999).
44. C. R. Jarvis, T. R. Anderson, and R. D. Andrew, "Anoxic depolarization mediates acute damage independent of glutamate in neocortical brain slices," *Cereb. Cortex* **11**(3), 249–259 (2001).
45. I. Joshi and R. D. Andrew, "Imaging anoxic depolarization during ischemia-like conditions in the mouse hemi-brain slice," *J. Neurophysiol.* **85**(1), 414–424 (2001).
46. T. M. Polischuk, C. R. Jarvis, and R. D. Andrew, "Intrinsic optical signaling denoting neuronal damage in response to acute excitotoxic insult in the hippocampal slice," *Neurobiol. Dis.* **4**(6), 423–437 (1998).
47. C. R. Jarvis et al., "Interpretation of intrinsic optical signals and calcein fluorescence during acute excitotoxic insult in the hippocampal slice," *NeuroImage* **10**(4), 357–372 (1999).
48. A. Obeidat, C. R. Jarvis, and R. D. Andrew, "Glutamate does not mediate acute neuronal damage following spreading depression induced by O2/glucose deprivation in the hippocampal slice," *J. Cereb. Blood Flow Metab.* **20**(2), 412–422 (2000).
49. M. Friebel et al., "Influence of oxygen saturation on the optical scattering properties of human red blood cells in the spectral range 250 to 2000 nm," *J. Biomed. Opt.* **14**(3), 034001 (2009).

Keiichiro Yoshida is a PhD student in the Graduate School of Bio-Applications and Systems Engineering, Tokyo University of Agriculture and Technology, Japan, where he received his MS degree in engineering in 2012.

Izumi Nishidate is an associate professor in the Graduate School of Bio-Applications and Systems Engineering, Tokyo University of Agriculture and Technology. He received his MS and PhD degrees from Muroran Institute of Technology, Japan. His research interests include diffuse reflectance spectroscopy, light transport in biological tissues, multispectral imaging, and functional imaging of skin and brain tissues.

Tomohiro Ishizuka is a MS student in the Graduate School of Bio-Applications and Systems Engineering, Tokyo University of Agriculture and Technology, Japan.

Satoko Kawauchi is an assistant professor in the Division of Biomedical Information Sciences, National Defense Medical College Research Institute, Japan. She completed her MS degree at Keio University and received a PhD degree in medicine from Kyorin University, Japan. Her research interests encompass functional imaging of brain, photodynamic therapy, and diagnosing/imaging tissue viability using light scattering.

Shunichi Sato is an associate professor in the Division of Biomedical Information Sciences, National Defense Medical College Research Institute, Japan. He received his MS and PhD degrees from Keio University, Japan. His research interests include photomechanical waves and their application to gene/drag delivery systems, photoacoustic imaging, photodynamic therapy, as well as diagnosing/imaging brain tissue viability.

Manabu Sato is a professor in the Graduate School of Science and Engineering, Yamagata University, Japan. He received his MS and PhD degrees from Tohoku University, Japan. His research focus is on optical coherence tomography, spectral imaging, and their applications to imaging of intrinsic optical signals in brain, as well as development of instruments with optical fiber for biological tissues.